ICAS 2020 SHANG HAI
International Council of the Aeronautical Sciences
32nd Congress of the International Council of the Aeronautical Sciences
September 6-10, 2021
Pudong Shangri-La, Shanghai, China

EXPERIMENTAL INVESTIGATION ON FLOW CHARACTERISTICS IN COMPRESSOR ACOUSTIC-CAVITY RESONANCE TEST FACILITY BY PIV

Zhang Zhibo, Yang Mingsui, Wu Hui, Wang Meng

AECC Shenyang Engine Research Institute, Shenyang 100015, China

Abstract

Flow fields were measured by Particle Image Velocimetry (PIV) in a compressor acoustic-cavity resonance test facility at different mass flow conditions. The steady and unsteady flow characteristics of velocity and vorticity fields were compared. Moreover, the relationships between the high-order statistics and resonance were analyzed in the quantitative method. It is hoped that the research results can provide some support for exploring the physical mechanism of compressor cavity resonance. The results show that: the shedding vortex is formed after the first stage disk, and the flow pattern alters as the variation of mass flow conditions; when acoustic-cavity resonance occurs, the instantaneous forms of shedding vortex are more similar with each other, meanwhile, the frequencies of shedding vortex, being closed to the frequency of pressure fluctuation when resonance occurs, concentrate mainly from 1100 to 1300 Hz, which means the form and frequency of shedding vortex are closely related with acoustic-cavity resonance phenomenon; by analyzing different high-order statistics, it is also found that the Reynolds stress $\rho\overline{v'v'}$ grows up greatly as the resonance occurs, which indicates the momentum exchange along the radial direction between the shedding vortex and the surrounding fluid is closely related to the resonance phenomenon of the acoustic cavity.

Keywords: compressor; acoustic-cavity resonance; turbulent fluctuation; shedding vortex; Particle Image Velocimetry

1. General Introduction

With the design requirements of high pressure ratio and high efficiency, compressor blades often work under high load conditions. Combined with aerodynamic, structural and acoustic loads, the compressor blades often have excessive vibration and even fatigue fracture, which have a significant impact on engine safety and reliability [1]. In recent years, a kind of acoustic cavity resonance phenomenon leading to blade fatigue failure has been found in the actual operation of compressor, which provides a new research idea for further analysis of blade fatigue fracture mode under gas solid interaction [2-4].

The physical essence of cavity resonance is fluid-induced vocalization [5-8]. Rossiter et al. proposed that the flow splits at the upstream sharp edge and the shear layer moves downstream [9]. The disturbance gradually enlarges and eventually impacts the downstream sharp edge. Rockwell et al. proposed that the boundary layer of incoming flow separates at the sharp edge upstream of the cavity, which will cause periodic fluctuations of velocity and pressure due to the instability of the shear layer [10]. Powell et al. pointed out that under certain conditions, fluid vortex motion and sound waves can be transformed into each other, accompanied by the transformation of vortex energy and sound energy [11].

In recent years, CFD has been used more and more in the study of acoustic cavity resonance phenomenon [12-14]. However, because the accuracy of CFD simulation is affected by turbulence model and other factors, it is still necessary to be verified by the experimental results[12]. In addition, the experimental research on the acoustic resonance phenomenon is mainly to study the pressure pulsation characteristics in the acoustic cavity resonance mode, but the measurement results of the internal flow field structure are very limited.

In this paper, flow fields were measured by Particle Image Velocimetry (PIV) in a compressor

acoustic-cavity resonance test facility at different mass flow conditions. The steady and unsteady flow characteristics of velocity and vorticity fields were compared. Moreover, the relationship between the high-order statistics and resonance was analyzed by the quantitative method. It is hoped that the results will provide some supports for the exploration of critical parameters for compressor acoustic-cavity resonance phenomenon and the inner physical mechanism.

2. Test Facility and Measurement Methods

2.1 Testing Facility

The test is carried out on the compressor acoustic-cavity resonance test facility of Shenyang engine research institute. As shown in Figure 1, the test facility includes two-stage wheel disc, hub and shroud. The shroud is processed with plexiglass, which is convenient for PIV measurement. A circular cavity is formed by two-stage wheel disc, hub and shroud. The cross-sectional dimension of the cavity is 75mm × 52mm, and the distance between the top of the wheel disc and the gearbox is 11mm. During the test, the air flows from the inlet, enters the disk cavity of the test facility after passing through the first stage disk, and finally flows out from the flow path at the top of the second stage disk. It is necessary to point out that the wheel is stationary in this paper.

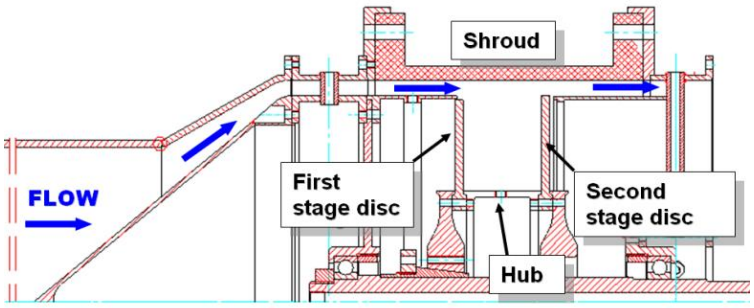

Figure 1 – Schematic of Compressor Acoustic-Cavity Resonance Test Facility

2.2 Measurement System

The dynamic pressure was measured using a Kulite micro dynamic pressure sensor with a collection frequency of 25 KHz. The dynamic pressure was collected and analyzed using the HGL dynamic measurement and analysis platform.

The PIV measurement system developed by Lavision is adopted for velocity measurement. The CCD adopts ImagerProPlus/ProX4M (2048 × 2048 Pixels, 12 bits), the acquisition frequency is 2.0 Hz, and the measurement and analysis software is DAVIS 8.1. The tracer particles of PIV are generated by the combustion type solid particle generator developed by the research group and distributed in the inlet pipe of the test device.

3. Test and Data Processing Methods

3.1 Pressure Measurement Scheme

The test is carried out on the compressor acoustic-cavity resonance test facility of Shenyang engine research institute. As shown in Figure 1, the test facility includes two-stage wheel disc, hub and shroud. The shroud is processed with plexiglass, which is convenient for PIV measurement. A circular cavity is formed by two-stage wheel disc, hub and shroud. The cross-sectional dimension of the cavity is 75mm × 52mm, and the distance between the top of the wheel disc and the gearbox is 11mm. During the test, the air flows from the inlet, enters the disk cavity of the test facility after passing through the first stage disk, and finally flows out from the flow path at the top of the second stage disk. It is necessary to point out that the wheel is stationary in this test.

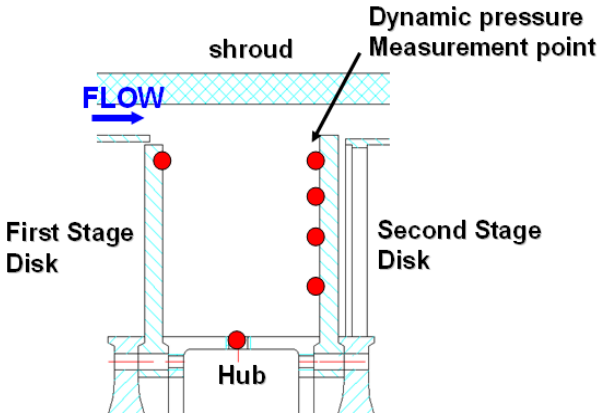

Figure 2 – Locations of dynamic pressure measurement points

3.2 PIV Measurement Scheme

The velocity field is measured by two-dimensional PIV, and the system layout is shown in figure 3. The laser is introduced directly above the test equipment through the optical arm. The CCD camera is placed on the side of the test equipment through the tripod. Both CCD and laser are connected to the time series controller (PTU), and the acquisition trigger signal is sent out by PTU.

Due to the influence of the surface reflective, obtained by PIV flow field of the real effective area will be reduced. Figure 4 shows the measurement of effective area. It can be seen from the figure that this area completely covers most of the cavity and the area with strong mixing between the mainstream channel and the cavity, and can meet the measurement requirements. The measurement results include velocity *U* and *V* in two directions corresponding to the velocity components in *x* and *y* directions respectively.

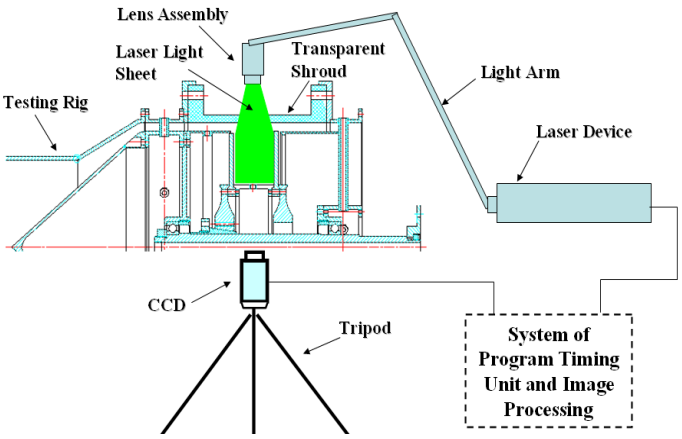

Figure 3 – Schematic of PIV Measurement System

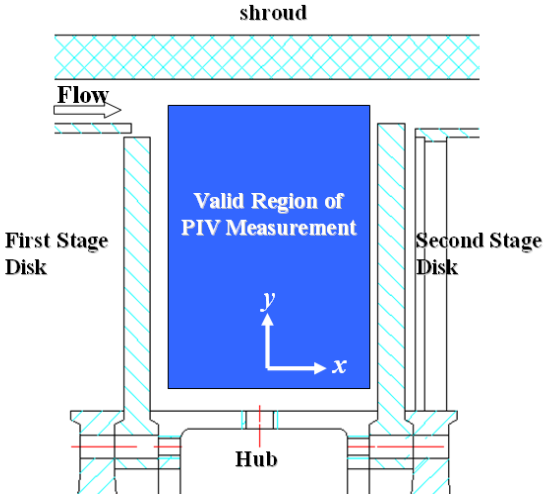

Figure 4 – Valid Measurement Region by PIV

3.3 Measurement conditions

During the test, the resonance is judged according to the pressure pulsation measured by the dynamic pressure sensor. When resonance occurs, the frequencies measured by the six dynamic pressure sensors are all concentrated at 1094 Hz.

In order to compare the difference of flow field between resonance and non-resonance test states, five working conditions were selected for PIV measurement, including condition 1 (flow rate 0.200kg/s, non-resonance state), condition 2 (flow rate 0.437kg/s, just entering resonance state), condition 3 (flow rate 0.447kg/s, fully entering resonance state), condition 4 (flow rate 0.459kg/s, just leaving resonance state) and condition 5 (flow rate 0.550kg/s, non-resonance state).

Table 1 – Tested operating conditions

Operating conditions	1	2	3	4	5
Mass flow rate Kg/s	0.200	0.437	0.447	0.459	0.550

3.4 Data processing method

This PIV data acquisition and processing adopts Davis 8.1 system of lavision company, which can apply advanced adaptive query domain and self-calibration algorithm, greatly improving the effective data rate and measurement accuracy of measurement results. The post-processing program developed by the research group is used to analyze the high-order turbulence field of the measurement data, which can analyze the effective data rate, vorticity, Reynolds stress, turbulent kinetic energy and other parameters. The main system setting parameters during data processing are shown in table 2.

Table 2 – Setup of PIV data processing parameters

Window Size	32 Pixel×32 Pixel
Overlap	50%
Algorithm	Muti-Grid
Spatial Resolution	1.16 mm×1.16 mm
Sample Number	600

4. Test Results and Analysis

4.1 Velocity field distribution

Figure 5 shows the distribution of the average axial velocity field in working conditions 1-5. It can be seen that under each working condition, with the increase of the flow rate, the flow velocity of the fluid above the cavity gradually increases, and the corresponding swirl velocity within the cavity also increases. It can be seen from the comparison of different working conditions that the characteristics of velocity distribution are very close, and the difference mainly lies in the magnitude of velocity. From the distribution of the flow field, it is easy to know that in different working conditions, there are circular vortices whose scale almost occupies the whole cavity. Moreover, the axial velocity gradient between the flow path above the cavity and the cavity is large, indicating that the region has obvious shear flow characteristics.

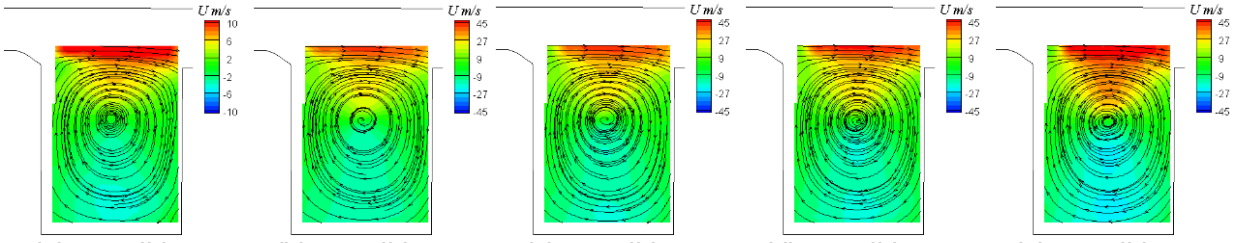

(a) Condition 1 (b) Condition 2 (c) Condition 3 (d) Condition 4 (e) Condition 5

Figure 5 – Distribution of ensemble-averaged axial velocity

Figure 6 shows the typical distribution of the transient axial velocity field in working condition 3 at different moments. It can be seen that the area of the high-velocity fluid above the cavity is always changing at different moments, indicating that the flow above the cavity has obvious unsteady fluctuation, and the vortex center of the annular cavity also oscillates with this phenomenon. The law of the other four working conditions is consistent with that of condition 3, and it is not described here.

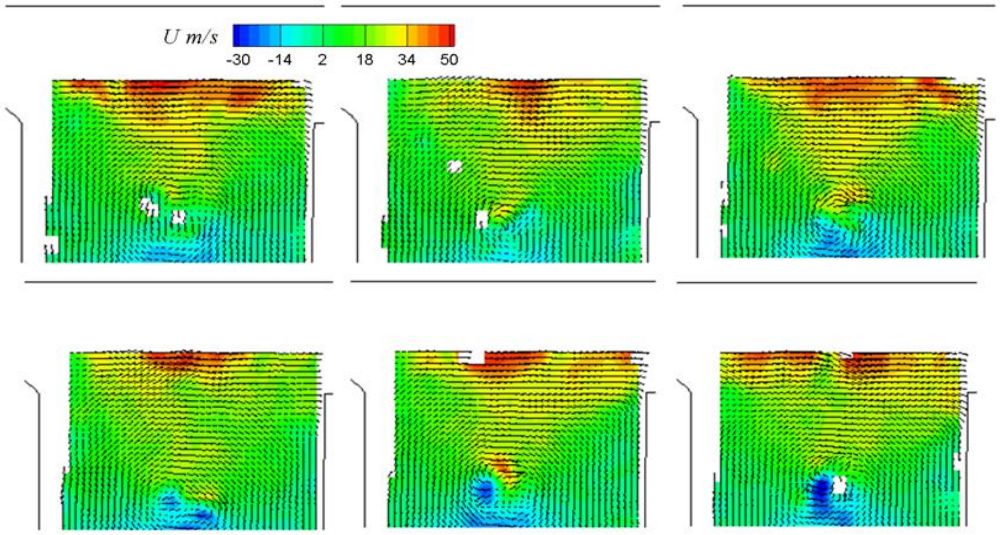

Figure 6 – Typical distribution of instantaneous axial velocity at operating condition 3

4.2 Vorticity field distribution

Vorticity is an important physical quantity reflecting fluid vortex and shear effect. Based on the PIV measurement results, the vorticity component based on the direction of the vertical measurement section is given in this section (see formula 1). Because the test device is axisymmetric, it is easy to know that the vorticity direction of large-scale circular vortices in the cavity is generally perpendicular to the measured cross section. The analysis of the vorticity in this direction can capture the main vortex characteristics.

$$\omega_z = \frac{\partial U}{\partial y} - \frac{\partial V}{\partial x} \tag{1}$$

Figure 7 shows the average vorticity field distribution. It can be seen from the figure that there is a very significant negative vorticity region at the center of the cavity under different working conditions, which is obviously caused by the circular vorticity in the cavity. Between the cavity and the main flow path, the axial velocity shear is more significant, and there is also a band with concentrated negative vorticity.

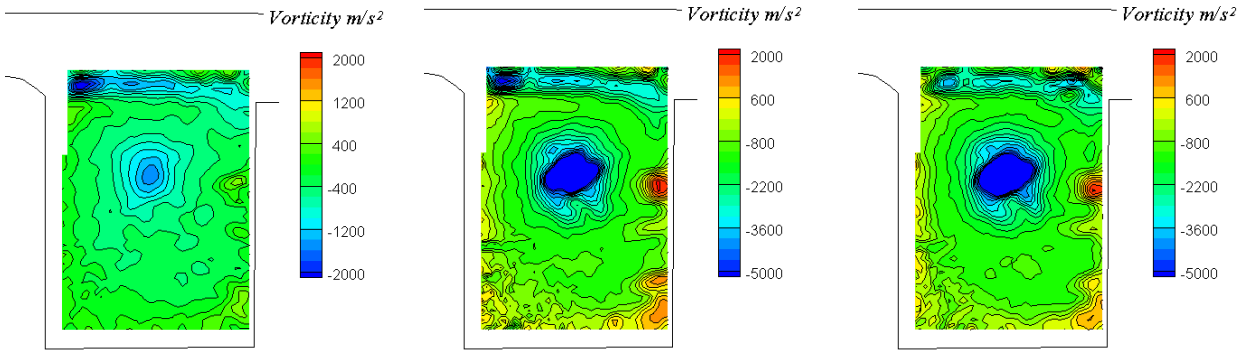

(a) Operating condition 1 (b) Operating condition 2 (c) Operating condition 3

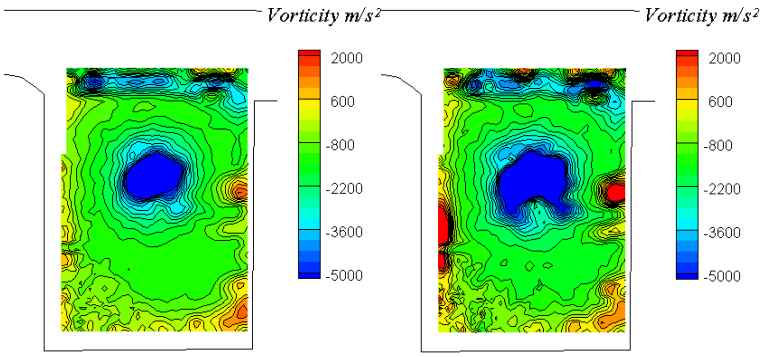

(d) Operating condition 4 (e) Operating condition 5

Figure 7 – Distribution of ensemble-averaged vorticity

It is well known that the main reason for introducing vorticity is the existence of velocity gradient. Vortices and shear flows similar to the boundary layer can be introduced with obvious concentrated vorticity. Simply using vorticity cannot fully determine the vortex shape of the flow, and more strict judgment criteria are needed to identify the vortex flow. According to previous research results, the commonly used vortex identification criteria including Q criteria, λ_2 criteria and Δ criterion, etc. The experimental data processing applied the λ_2 criterion (formula 2) for two-dimensional PIV results derived by Professor Liu Baojie from Beihang University [15]:

$$\lambda_2 = \left(\frac{\partial U}{\partial x}\right)^2 + \left(\frac{\partial V}{\partial y}\right)^2 + 2 \cdot \frac{\partial U}{\partial y}\frac{\partial V}{\partial x} \le 0 \tag{2}$$

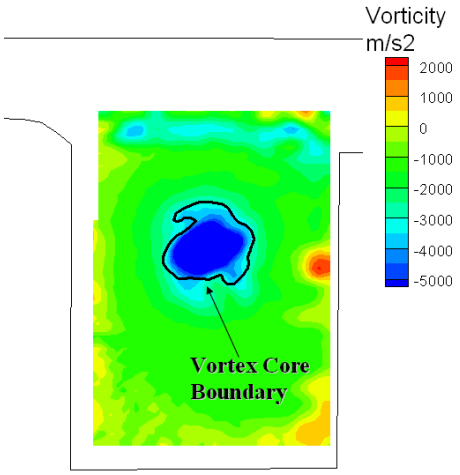

Figure 8 – Vortex core boundary distinguished by λ_2 criterion from ensemble-averaged flow fields (operating condition 3)

This criterion has been applied to the identification and judgment of the leakage vortex in the compressor, and the structure of the rotor tip leakage vortex and other vortex systems can be well identified [16]. Figure 8 shows the vortex characteristics in the test facility at condition 3 identified by this criterion. The black thick solid line is the boundary of the vortex core identified by this method. It can be seen that λ_2 criterion can identify the concentrated vortex in the center of the cavity, and it is in good agreement with the region with strong negative vorticity. It can also be seen from the figure that for the mean field, only the large-scale concentrated vortices existing in the center of the cavity can be identified, while the real flow is highly unsteady. Therefore, this method will be used to analyze the characteristics of the vortex in different transient measurement results.

Figure 9 shows the typical transient vorticity field distribution in conditions 1, 3, and 5. The solid black lines in the figure indicate the vortex core boundary identified by λ_2 criterion. According to the distribution of transient field, there is an obvious concentrated vortex in the center of the cavity under different working conditions and it swings back and forth around the center. In the region with strong velocity shear between the main flow path and the cavity, the fluid moves downstream in the form of a shedding vortex, which is the main flow mechanism leading to the existence of strong negative

vorticity in the region, and the flow has significant unsteady characteristics, so the vortex structure cannot be identified in this region in the mean field.

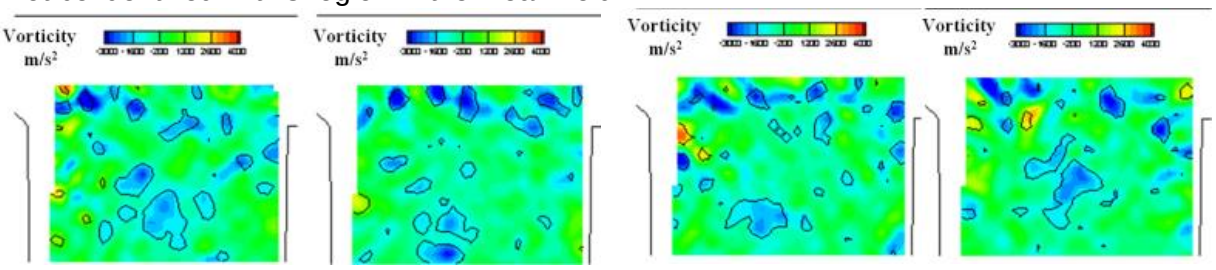

(a) Condition 1

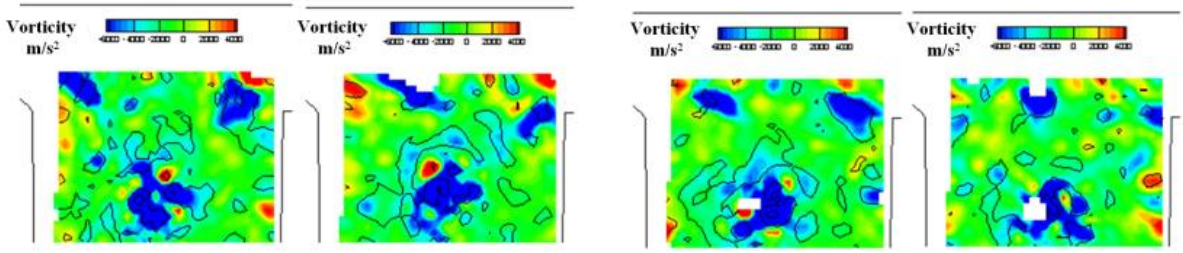

(b) Condition 3

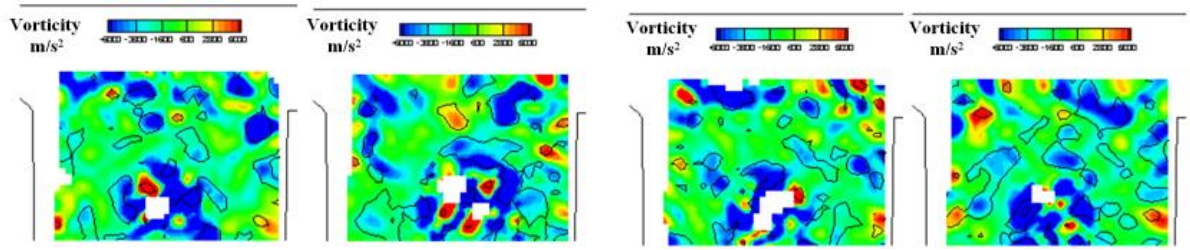

(c) Condition 5

Figure 9 – Typical distribution of instantaneous vorticity fields (black solid line curve indicates the vortex core boundary)

In the condition of small flow (condition 1), the scale of shedding vortex is small, and according to the number of shedding vortices in a transient vorticity field, the shedding frequency of shedding vortex is high; in the state of complete resonance (condition 3), the scale and strength of shedding vortex (judging from the size of vorticity) are obviously increased, and the main shedding vortex shedding frequency is significantly reduced; in the condition of large flow (condition 5), it can be seen that there are still large-scale shedding vortices appearing in condition 3, but other scale shedding vortices and induced vortices caused by shedding vortices are also significantly increased. According to Fig. 10, it can be seen that when the shedding vortex is propagating downstream, it will hit the secondary disk, which will cause strong unsteady disturbance. By analyzing the transient field of condition 3, it can be seen that there are mostly two large-scale main shedding vortices in the measured field of view. According to the transient velocity field and the distance between two adjacent shedding vortices, it can be roughly calculated that the shedding frequency of the vortices under this condition is about 1100～1300 Hz as shown in figure 10, which is close to the main pressure fluctuation frequency (f = 1094 Hz) in the cavity at resonance measured by the dynamic pressure sensor.

In conclusion, when resonance occurs, the shedding vortex will propagate to the downstream with large-scale vortex with relatively concentrated vortex form, and hit the secondary disk. The shedding frequency of the shedding vortex is close to the pressure fluctuation frequency measured on the disk when the cavity resonates. It can be inferred that the unsteady pulsation caused by the vortex shedding and the interaction with the surrounding fluid and the wheel disk may be the main physical mechanism of resonance in the test facility.

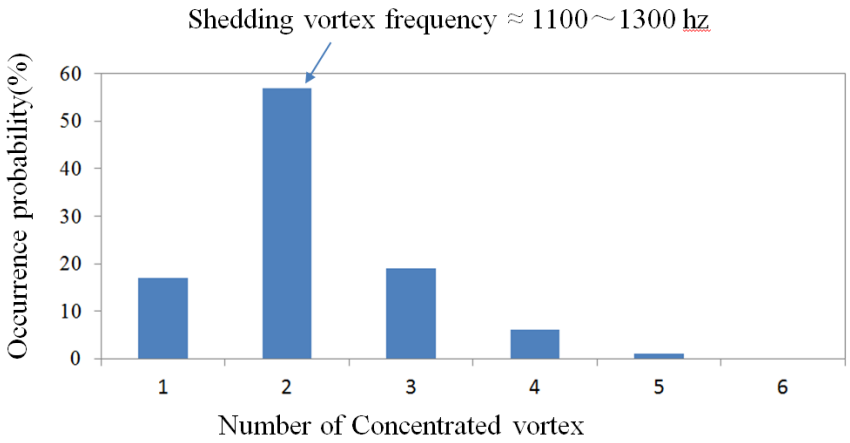

Figure 10 – Probability of the number of Shedding vortex at Condition 3

4.3 Distribution of higher-order statistics

The flow in the test facility has obvious unsteady flow characteristics, especially in resonance and non-resonance state, the vortex structure also has certain changes. In order to further analyze the differences of different flow patterns, the distribution of higher-order statistics will be analyzed as follows.

$$\frac{D}{Dt}\left(\frac{1}{2}U_iU_i\right)=\frac{\partial}{\partial x_j}\left(-\frac{P}{\rho}U_j+2\nu U_iS_{ij}--\overline{u_i'u_i'}U_i\right)-2\nu S_{ij}S_{ij}+\overline{u_i'u_j'}S_{ij} \quad (3)$$

Formula 3 is the mechanical energy transport equation of the incompressible fluid, where U_i represents the velocity component of the fluid in i direction, $S_{ij}(S_{ij}=0.5\cdot\left(\partial U_i/\partial x_j+\partial U_j/\partial x_i\right))$ represents the strain rate tensor of the average motion. The variable u_i' represents the velocity of the fluid in i direction.

According to formula (3), the transport term of average kinetic energy includes the transport of average pressure to mechanical energy$\left(\partial(-PU_j/\rho)/\partial x_j\right)$, Transport of mechanical energy by mean viscous forces of motion $\left(\partial(2\nu U_iS_{ij})/\partial x_j\right)$ and Transport of mechanical energy by turbulent pulsation($\partial(-\overline{u_i'u_i'}U_i)/\partial x_j$). At the same time, viscous and turbulent mixing also involves dissipation of mechanical energy$-2\nu S_{ij}S_{ij}+\overline{u_i'u_j'}S_{ij}$. In this study, the region of the shedding vortex is far away from the central vortex core in the cavity, and the influence of the pressure gradient is limited; the turbulence fluctuation and the mixing effect are usually more than one order of magnitude larger than the influence of viscosity, which is the main reason for the mechanical energy transport and loss. Therefore, the following focuses on the analysis of physical quantities related to turbulence pulsation.

The higher-order statistics related to turbulence include turbulence intensity, turbulence kinetic energy and Reynolds stress. In this measurement, due to the small velocity in some areas (such as the center of vortex core in the cavity), the value of the turbulence tends to be very large, which is not convenient for analysis. However, turbulence kinetic energy and Reynolds stress respectively represent the energy intensity of turbulence fluctuation and the stress components that contribute to turbulence fluctuation. Therefore, the following analysis focuses on the distribution characteristics of turbulence kinetic energy and Reynolds stress.

Considering the reasonable comparison of the changes of high-order measurement in different flow states, this paper makes dimensionless treatment of high-order statistics. The specific expressions are shown in formula 4 and formula 5:

$$(T_k)_{noml}=\frac{(u'^2+v'^2+w'^2)}{2\cdot U_{in}^2} \quad (1)$$

$$\left(\rho\overline{u_i'u_j'}\right)_{noml}=\frac{\rho\overline{u_i'u_j'}}{\rho U_{in}^2} \quad (2)$$

Where U_{in} is the average velocity in the flow path between the disk and the casing before entering the cavity. It should be pointed out that the normal velocity W cannot be obtained in this measurement. Therefore, the components related to the pulsating velocity W 'are missing in the high-

order statistics.

Figure 11 shows the distribution of dimensionless turbulent kinetic energy. It can be seen that the characteristics of turbulent kinetic energy distribution under different working conditions are as follows: there is a region with very high turbulent kinetic energy in the center of the cavity, which is caused by the circular concentrated vortex swinging back and forth in the center of the cavity. It can be seen from the comparison of different conditions that with the increase of inlet flow, the range of high turbulent kinetic energy region expands and the value also increases. There are bands of high turbulent kinetic energy in the area where the shedding vortex is located above the cavity, and the value of turbulent kinetic energy is smaller than that in the area where the vortex is concentrated in the cavity. According to the analysis in the previous section, the physical mechanism that causes the high turbulent kinetic energy in this region is the unsteady oscillation in the downstream propagation of the shedding vortex. With the radial migration of the shedding vortex, the radial scale of the high turbulence region caused by the shedding vortex becomes larger and larger, and the radial scale of the corresponding high-turbulence kinetic energy region gradually expands along the axial direction. Moreover, with the increase of mixing, the corresponding turbulence dissipation increases, and the value of turbulent kinetic energy gradually decreases along the axial direction. When the inlet flow rate increases, the turbulent kinetic energy of the region where the shedding vortex is located is gradually increased, in which conditions 2, 3 and 4 are in the resonance region (the flow rate is very close), and the turbulent kinetic energy is relatively close, which is significantly greater than that of condition 1, while condition 5 has a larger flow rate, and the turbulent energy of the corresponding region is also significantly greater than that of the other four conditions.

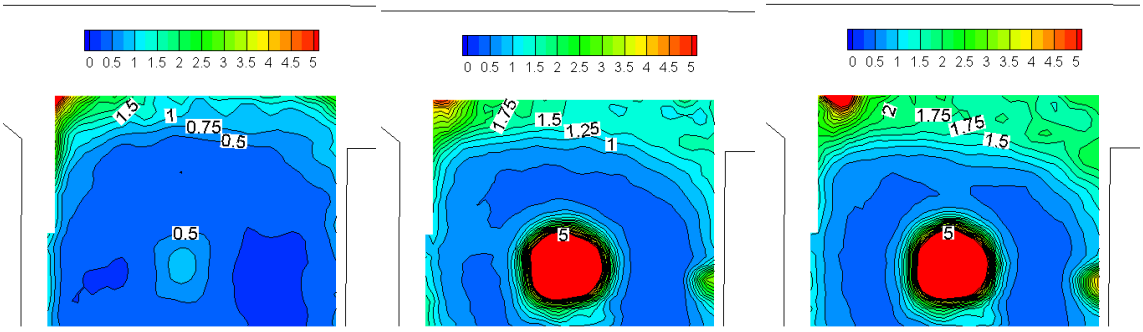

(a) Condition 1 (b) Condition 2 (c) Condition 3

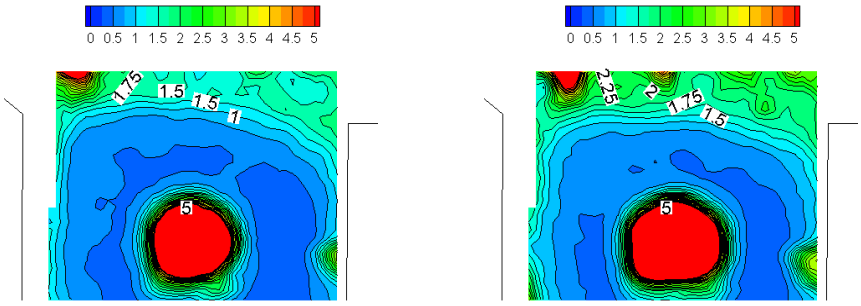

(d) Condition 4 (e) Condition 5

Figure 11 – Distribution of normalized turbulent kinetic energy

Compared with conditions 2-4, the turbulent kinetic energy of condition 2 and condition 4 is relatively close. The turbulent kinetic energy of condition 3 (in the fully resonant state) in the shedding vortex region is higher, which is increased by about 15% in the upstream and about 50% in the downstream compared with condition 2 and condition 4, which indicates that the turbulence fluctuation in the region is stronger and less easily dissipated in the fully resonant state.

The characteristics of Reynolds stress variation closely related to turbulent mixing will be further analyzed as follows. Figure 12 shows the distribution of dimensionless Reynolds normal stress $\left(\rho\overline{u'u'}\right)_{noml}$. According to the analysis of the results of each working condition, its distribution characteristics are similar to the turbulent kinetic energy. Generally, with the development of the shedding vortex to the downstream, the higher radial scale gradually expands and the value

decreases; with the increase of the inlet flow, the turbulence mixing in the region where the shedding vortex is located increases. It should be pointed out that under the resonance condition 2-4, the distribution change of Reynolds normal stress $\left(\rho\overline{u'u'}\right)_{noml}$ is not obvious, only the radial scale is slightly enlarged, but the strength is relatively close.

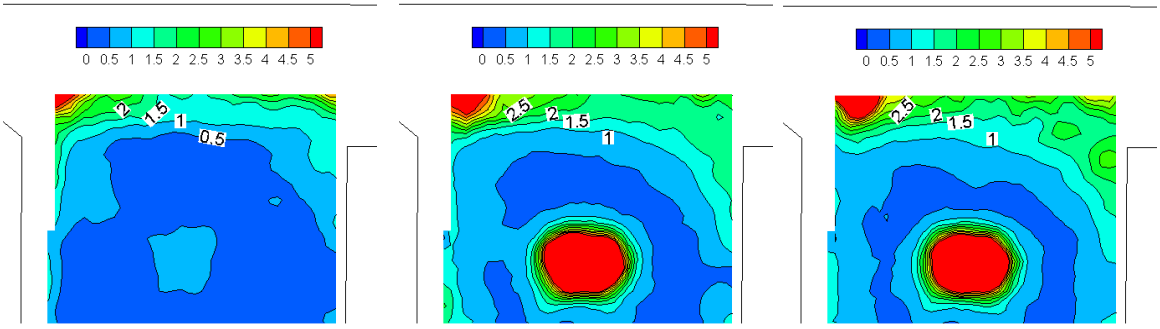

(a) Condition 1 (b) Condition 2 (c) Condition 3

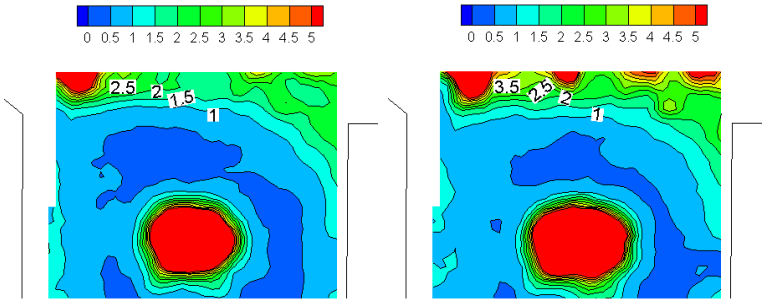

(d) Condition 4 (e) Condition 5

Figure12 – Distribution of normalized Reynolds normal stress $\left(\rho\overline{u'u'}\right)_{noml}$

Figure 13 shows the distribution of dimensionless Reynolds normal stress$\left(\rho\overline{v'v'}\right)_{noml}$, the value of which is close to$\left(\rho\overline{u'u'}\right)_{noml}$, and the turbulent mixing effect increases with the increase of flow rate. The distribution trend is similar to the higher-order statistics of the previous analysis, but the distribution is quite different from the previous results in the state of complete resonance, which is mainly reflected in the significant increase of the radial Reynolds normal stress in condition 3, which is about 30% - 40% higher in the upstream than in condition 2 and condition 4, and in the downstream area, the value even increases by more than 100% compared with the other two conditions. The radial Reynolds normal stress $\left(\rho\overline{v'v'}\right)_{noml}$ is slightly larger than that in case 5 with larger flow rate. Therefore, it can be seen that in the flow state of complete resonance, the main change is that the Reynolds normal stress of the fluid in the region where the shedding vortex is located increases significantly along the radial direction.

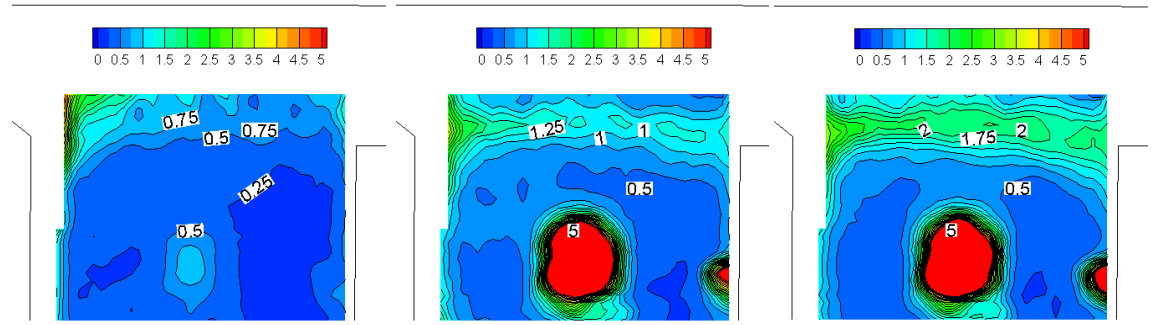

(a) Condition 1 (b) Condition 2 (c) Condition 3

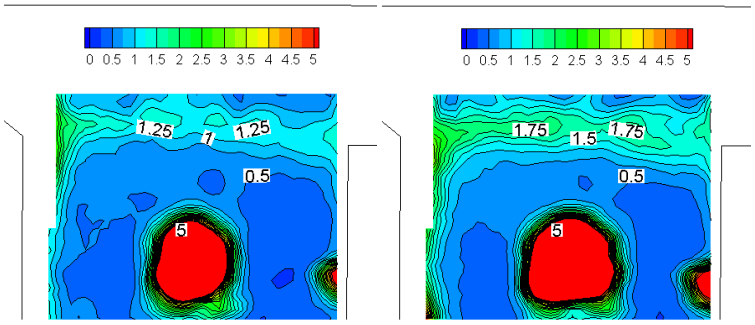

(d) Condition 4 (e) Condition 5

Figure13 – Distribution of normalized Reynolds normal stress $\left(\rho\overline{v'v'}\right)_{noml}$

Figure 14 shows the distribution of dimensionless Reynolds shear stress $\left(\rho\overline{u'v'}\right)_{noml}$.The shear stress in the region where the shedding vortex is located increases by about 20% - 30% in condition 3 compared with condition 2 and condition 4, and is close to that in condition 5. However, compared with the other two Reynolds normal stress results, the Reynolds shear stress in this direction is relatively small, about 40% - 60% of the other two Reynolds normal stress components.

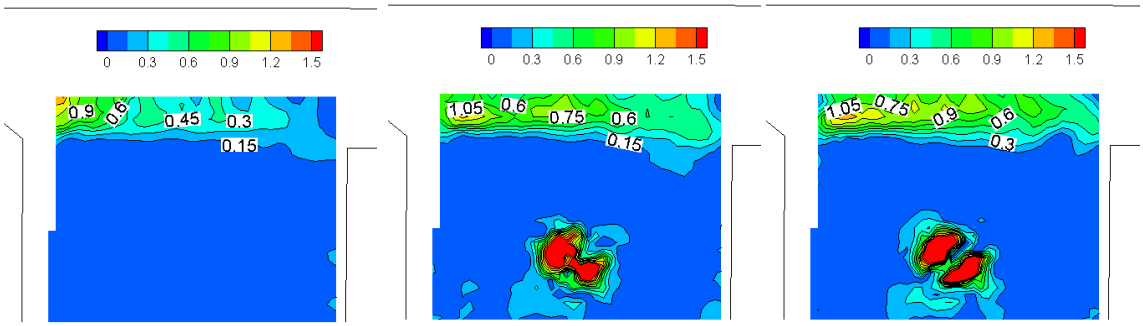

(a) Operating condition 1 (b) Operating condition 2 (c) Operating condition 3

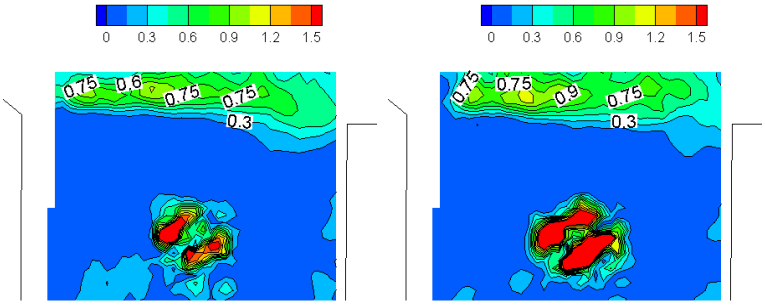

(d) Operating condition 4 (e) Operating condition 5

Figure14– Distribution of normalized Reynolds shear stress $\left(\rho\overline{u'v'}\right)_{noml}$

5. Conclusion

In this paper, through the detailed flow field measurement and analysis in compressor acoustic-cavity resonance test facility, the following main conclusions are obtained:

(1) Under different working conditions, the overall flow structure in the test facility is basically similar. After the air flows into the cavity, the oscillating shedding vortex is formed, which not only propagates along the axial direction, but also migrates along the radial direction, and hits the downstream secondary stage wheel disc.

(2) The shedding vortex pattern changes under different working conditions. At small flow condition away from resonance, the strength of shedding vortex is weak and the scale is small. At the condition of large flow away from resonance, the strength of shedding vortex is obviously enhanced, and it is accompanied by shedding vortex and induced vortex of different scales. In the case of resonance, the shedding vortices in each transient flow field are closer in shape, mostly in the form of large-scale vortices, and the shedding frequencies are concentrated.

(3) Under the condition of complete resonance, according to the PIV transient results, the main shedding vortex frequency is about 1100-1300 Hz, which is close to the pressure fluctuation frequency 1094 Hz measured during cavity resonance. The unsteady shedding process of shedding vortex and the resulting interaction with surrounding flows and wheel disk may be closely related to cavity resonance;

(4) When entering the complete resonance state, the Reynolds normal stress $\rho\overline{v'v'}$ in the region where the shedding vortex is located increases obviously. Compared with the results just entering and leaving the resonance state, the $\rho\overline{v'v'}$ increases by 30% - 100%, indicating that the momentum exchange along the radial direction of the flow increases significantly.

6. Contact Author Email Address

Mailto: zhibo346@163.com

7. Copyright Statement

References

[1] Lin Z M, Li K A, Yang S Q. Experimental research on sound waves excitation to aero-engine compressor rotor blade . Journal of dynamics and control, Vol.8, No.1: pp12-18, 2000.

[2] Kaji S, Okazaki T, Propagation of sound waves through a blade row: II. Analysis based on the acceleration potential method. Journal of Sound and Vibration, Vol.11, No.3, pp 355-375, 1970.

[3] Kielb R. E., Blade Excitation by Aerodynamic Instabilities-A Compressor Blade Study. ASME Paper, No. GT2003-38634, 2003.

[4] Camp T R, A Study of Acoustic Resonance in a Low-Speed Multistage Compressor. ASME J. Turbomach, Vol.121, pp 36-43, 1999.

[5] Ma R, Slaboch P E, Morris S C. Fluid mechanics of the flow-excited Helmholtz resonator. Journal of Fluid Mechanics, Vol.623, pp 1-26, 2009.

[6] Chu B T, Kovasznay L S G. Non-linear interactions in a viscous heat-conducting compressible gas. Journal of Fluid Mechanics. Vol.3, pp 494-514, 1958.

[7] Batchelor G K. An Introduction to Fluid Dynamics. 1st edition, Cambridge University Press, 1967.

[8] Drazin P G. Hydrodynamic Stability. 1st edition, Cambridge University Press, 2004.

[9] Rossiter J E. Wind tunnel experiments on the flow over rectangular cavities at subsonic and transonic speeds. Aeronautical Research Council Reports and Memoranda, Report No. 64037, 1964

[10] Rockwell D, Lin J, Oshkai P, et al. Shallow cavity flow tone experiments: onset of locked-on states. Journal of Fluids and Structures. Vol17, No.3, pp 381-414, 2003.

[11] Powell A. Theory of vortex sound. Journal of the Acoustical Society of America. Vol36,No.1, pp 177-195,1964,

[12] Ricot D, Maillard V, Bailly C. Numerical simulation of the unsteady flow past a cavity and application to the sunroof buffeting. AIAA, Netherland, No. 2001-2112, 2001.

[13] Mallick S, Shock R, Yakhot V. Numerical simulation of the excitation of a Helmholtz resonator by a grazing flow. Journal of the Acoustical Society of America. Vol.114, No.4, pp 1833-1840, 2003.

[14] Inagaki M, Murata O, Kondoh T, et al. Numerical prediction of fluid-resonant oscillation at low Mach number. AIAA Journal, Vol. 40, No. 9, pp 1823-1829, 2002.

[15] Liu B J. PIV study of airfoil near wake flow part Ⅱ—dynamic mechanism. Journal of aerospace power. Vol. 14, No.2, pp 125-130, 1998

[16] Zhang Z B, Xian J Y, Liu B J, Characteristics of the tip leakage vortex in a low-speed axial compressor with different rotor tip gaps. ASME, GT2012-69148, pp 311-322, Copenhagen, 2012.